ACS APPLIED MATERIALS & INTERFACES

Research Article

Cite This: ACS Appl. Mater. Interfaces 2019, 11, 1529−1537

www.acsami.org

Tuning the Magnetic Properties of FeCo Thin Films through the Magnetoelastic Effect Induced by the Au Underlayer Thickness

Luís Cabral,[†] Fermin H. Aragón,[‡] Leonardo Villegas-Lelovsky,[†,‡] Matheus P. Lima,[†] Waldemar A. A. Macedo,[§] and Juarez L. F. Da Silva*[,∥]

[†]Departamento de Física, Universidade Federal de São Carlos, 13565-905 São Carlos, São Paulo, Brazil

[‡]Núcleo de Física Aplicada, Instituto de Física, Universidade de Brasília, DF, Brasília 70910-900, Brazil

[§]Centro de Desenvolvimento da Tecnologia Nuclear, CDTN, 31270-901 Belo Horizonte, Minas Gerais, Brazil

[∥]São Carlos Institute of Chemistry, University of São Paulo, PO Box 780, 13560-970 São Carlos, São Paulo, Brazil

Supporting Information

ABSTRACT: Tuning the magnetic properties of materials is a demand of several technologies; however, our microscopic understanding of the process that drives the enhancement of those properties is still unsatisfactory. In this work, we combined experimental and theoretical techniques to investigate the handling of magnetic properties of FeCo thin films via the thickness-tuning of a gold film used as an underlayer. We grow the samples by the deposition of polycrystalline FeCo thin films on the Au underlayer at room temperature by a magnetron sputtering technique, demonstrating that the lattice parameter of the sub-20 nm thickness gold underlayer is dependent on its thickness, inducing a stress up to 3% in sub-5 nm FeCo thin films deposited over it. Thus, elastic-driven variations for the in-plane magnetic anisotropy energy, K_u, up to 110% are found from our experiments. Our experimental findings are in excellent agreement with ab initio quantum chemistry calculations based on density functional theory, which helps to build up an atomistic understanding of the effects that take place in the tuning of the magnetic properties addressed in this work. The handling mechanism reported here should be applied to other magnetic films deposited on different metallic underlayers, opening possibilities for large-scale fabrication of magnetic components to be used in future devices.

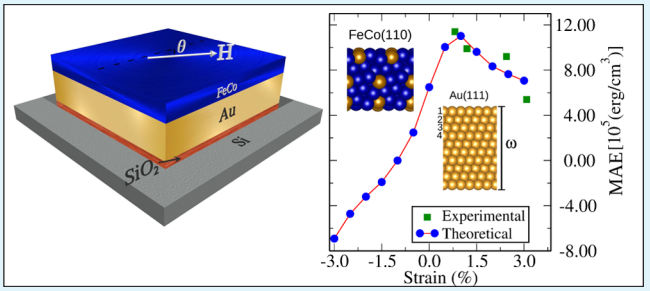

KEYWORDS: *magnetic properties, thin films, strain, ab initio calculations, FeCo, Au underlayer*

1. INTRODUCTION

Polycrystalline magnetic films have promising applications in several technological fields such as data storage media, sensors, and other devices.[1,2] Thus, several studies have been reported with the aim to control the magnetization, in particular, the tuning of the magnetic anisotropy hardness, which can be accessed by the study of the magnetic anisotropy energy, K_u.[3−5] The tuning of the magnetic anisotropy has been the focus of the scientific community in the last decades,[6] demonstrating the possibilities of a directional control of the hard axis by (i) cold-rolling, (ii) magnetic annealing under application of an external magnetic field, and (iii) magnetic quenching, in which the material is cooled below the Curie temperature, T_C, in the presence of a magnetic field.

Recently, several new methods for manipulation of the magnetic anisotropy are emerging, for instance, (i) magnetic anisotropy control by the obliquely underlayer deposition,[7] (ii) topography,[8] and (iii) application of an external electric field.[5] One additional possibility to tune the magnetic properties is the application of strain fields, which is present in many prominent applications, such as the enhancement of ferroelectricity in $BaTiO_3$ thin films,[9] controlling the magneto-optical response of $BiFeO_3$,[10] generating spin-currents in quantum spin Hall systems,[11] and the electric field survey exchange bias in a $Co_{90}Fe_{10}/BiFeO_3/SrRuO_3$/PMN-PT heterostructure under different tensile regimes.[12] Furthermore, the tuning of the strain provides the path to improve the efficiency of some technological nanodevices such as fuel cells, ionic batteries, and so forth.[13−15] However, our atomistic understanding of the interface is far from satisfactory, particularly because of the challenges to obtain a direct correlation between strain and the local environment as well as for the thickness-dependent stiffness.[16]

Hitherto, magnetic alloys are promising candidates for materials to integrate future magnetic devices because of the possibility to tune their magnetic properties and size during the growth process.[17] Among several possible combinations to obtain thin-film alloys, FeCo is considered a suitable choice because of its specific magnetic properties[6] such as large permeability and very high saturation magnetization.[18] Also, it

Received: August 26, 2018
Accepted: December 7, 2018
Published: December 7, 2018

DOI: 10.1021/acsami.8b14736
ACS Appl. Mater. Interfaces 2019, 11, 1529−1537

can be easily attached to noble-metal surfaces such as Au[19] and Ag.[20−22] In this context, Wu et al. employed first-principles density functional theory (DFT) calculations to understand the giant uniaxial magnetic anisotropy energy and magnetic moments in tetragonal FeCo alloys as a function of the alloy concentration.[23] The versatile templating and phase transformation of the tetragonal FeCo leads to the structure distortion which tunes its magnetic moment.[24] Recently, Li et al. summarized the research progress on the magnetic properties of tetragonal FeCo alloys.[25]

The influence of the underlayer substrate was investigated by Lu et al. using FeCo/Ru films (Ru-underlayer) obtained by sputtering deposition,[26] where they identified an increased magnetic anisotropy induced by the Ru-underlayer thickness. Furthermore, a similar result was obtained with a Ta-underlayer.[27] Along with that, Winkelmann et al. demonstrated that tetragonally distorted FeCo alloys grown on the Pd(001) film have a high saturation magnetization and a high uniaxial magnetic anisotropy energy for determined values of the lattice distortion and alloy composition.[28] These results demonstrate the influence of the underlayer in the magnetic properties of deposited thin films, opening a possibility for magnetic anisotropy handling. However, a clear understanding of the underlayer influence on the properties of deposited thin films is lacking in the literature. Thus, the combination of ab initio DFT calculations and experimental measurements has the potential to improve our atomistic understanding in this field.

The tuning of the magnetic properties opens the possibility of a fine optimization of some devices having FeCo alloys in their composition. For example, one can mention the enhancement of the microwave absorption properties, which is a challenge in FeCo−graphene capsules[29] and FeCo hybrid nanorings.[30] Concerning FeCo/Au systems, previous studies have investigated the magnetic properties such as the magnetization saturation and the magnetic anisotropy.[31] However, the influence of the Au underlayer on the magnetic properties of the overlayer alloy was not completely elucidated. Moreover, a special attention should be given to the interface effect, where the interdiffusion can occur.[27,32,33] In addition, the analysis of orbital magnetization and magnetic dipole moment is crucial to describe the K_u properties.[34] Because of the symmetry breaking, the K_u in thin films is strongly different from the bulk phase.[35] In particular, the complex endeavors to understand the magnetic properties of the nano-alloys with a strong magnetocrystalline anisotropy boosted applications in high density data storage devices,[36−40] where a high saturation magnetization is required for the writing and heading process, and also, a strong K_u to overcome the superparamagnetic limit.[41]

Here, we report experimental measurements combined with ab initio DFT calculations to understand the Au underlayer influence on the structural and magnetic properties of the $Fe_{20\%}Co_{80\%}$ (≈5 nm thickness) polycrystalline films. The FeCo/Au films were grown on Si substrates by the magnetron sputtering process with different Au underlayer thicknesses. We concluded that the lattice parameter of the Au-underlayer increases with the increase of underlayer thickness, which affects the strain of the FeCo alloy deposited over it. Stretches up to 3% were observed for the FeCo alloy. Additionally, we demonstrated a high dependence of the FeCo magnetic properties on the strain. Thus, summing these effects, the Au-underlayer thickness acts as a handling mechanism for the magnetic properties of the alloy deposited over it.

2. EXPERIMENTAL APPROACH

The FeCo (5 nm) thin films with gold thickness (ω) from 5 to 20 nm were deposited at room temperature by direct current (dc) magnetron sputtering process, at 8.6×10^{-3} mbar argon pressure, using the sputtering targets of $Fe_{20\%}Co_{80\%}$ (99.9%) and Au (99.9%) disks onto polycrystalline 1 cm × 1 cm silicon wafer. In order to study the structural properties of the thin films, by X-ray diffraction (XRD) measurements, no capping was introduced in the structure and, after the deposition, the samples were stored in vacuum environment to avoid oxidation process. XRD measurements were carried out on all the samples, using the commercial diffractometer Rigaku model Ultima IV, with Cu Kα radiation (λ = 1.541 Å).

To extract the structural parameters such as grain size, residual strain, bonding distances, d_{Fe-Co}, lattice parameters, a, as a function of the Au-underlayer thickness of both phases, we performed the Rietveld refinements on all grazing angle X-ray diffraction (GXRD) patterns. The Bragg reflections peaks shape was emulated using the Lorentzian function implemented within the GSAS (General Structure Analysis System) software,[42] where the full width at half maximum (fwhm), β, were accessed by the following equations: $\beta = Y \tan\theta + X/\cos\theta$ (where X and Y are refinements parameters).

The line broadening induced by the instrumental influence was improved by discriminating the standard sample-linewidth (Si single crystal) from the studied sample-one. Adopting that the final linewidth, β, is univocally related to the crystallite size, $\langle D\rangle$, and the residual strain, ε, through the equation

$$\beta \cos(\theta) = \frac{K\lambda}{\langle D\rangle} + 4\varepsilon \sin(\theta) \quad (1)$$

where K is a dimensionless factor that depends on the particle shape ($K \approx 0.9$ case of spherical one). The $\langle D\rangle$ and ε parameters can be estimated from the linear fit after plotting $\beta\cos(\theta)$ as a function of $\sin(\theta)$ (the Williamson−Hall plot). Further details are described in the Supporting Information.

The atomic force microscopy (AFM) was used to study the surface morphology for the FeCo (5 nm)/Au (5−20 nm) thin films. Room temperature hysteresis and magnetization versus the angle curves were carried out in order to determinate the magnetic dependence of the FeCo films with the gold seed layer thickness, using the commercial vibrating sample magnetometer system of the Lakeshore. Conversion electron Mössbauer spectroscopy (CEMS) measurement was carried out in order to study the dependence of the iron neighborhood as the increase of the gold thickness and magnetic preferential orientation.

3. THEORETICAL APPROACH AND COMPUTATIONAL DETAILS

Our ab initio calculations were based on spin-polarized DFT within the formulation proposed by Perdew−Burke−Ernzerhof (PBE) for the exchange−correlation energy functional,[43] which provide an accurate description of the physical properties addressed in this work such as alloys, lattice parameters, magnetic anisotropy energies, and so forth.[6,44−46] The Kohn−Sham equations were solved using the all-electron projected augmented-wave method,[47,48] as implemented in the widely used Vienna Ab initio Simulation Package (VASP), version 5.4.4.[49,50] The equilibrium geometries for all calculations were obtained using the scalar-relativistic approximation to describe the valence electrons, that is, spin−orbit coupling (SOC) was not taken into account for the valence states, however, the SOC within the non-collinear spin approach was considered to calculate the magnetic properties.[6] For all calculations, we employed a self-consistent electronic convergence criteria of 10^{-6} eV, while the optimized structures were obtained once the atomic forces are smaller than 0.010 eV Å^{-1} on all atoms.

DOI: 10.1021/acsami.8b14736
ACS Appl. Mater. Interfaces 2019, 11, 1529−1537

The ab initio modeling of the experimental problems addressed in this work is a challenge due to the presence of the FeCo-alloy/Au interface, and hence, we employed few insights from the experimental results to reduce the computational cost. For example, from experimental observations, Figure 1, the FeCo alloys are deposited on the face-centered cubic (fcc) Au(111) surface, and forms a body-centered cubic (bcc) structure stacked along the bcc[110] direction, that is, the FeCo-alloy is terminated by a FeCo(110) surface. Thus, to understand the effect of the number of layers on the lattice parameters of the Au(111) thin film, which is expected to affect the FeCo magnetic properties, we employed the repeated slab Au(111) geometry using a 1 × 1 surface unit cell, a vacuum thickness of 15 Å, and from 3 (4.07 Å thickness) up to 15 (28.5 Å thickness) layers in the slab.

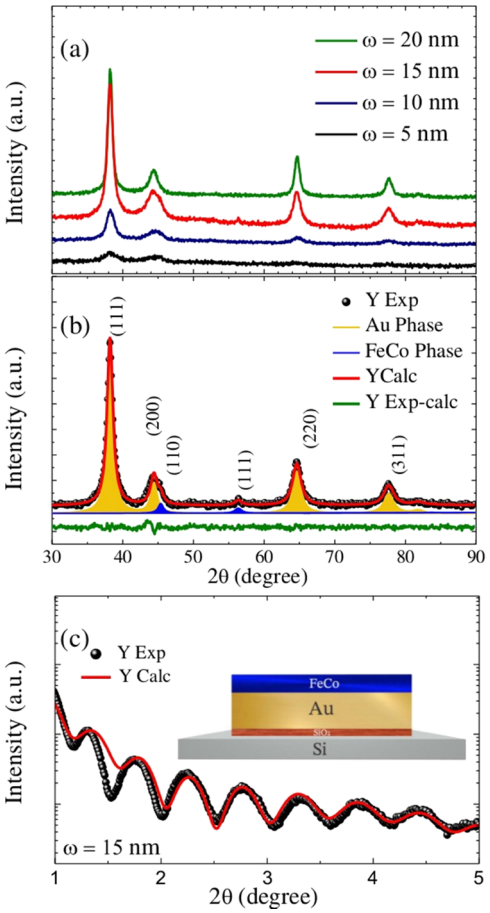

Figure 1. Panel (a) depicts the GIXRD of FeCo (5 nm)/Au (5−20 nm) thin-films. Panel (b) indicates the Rietveld refinement for the FeCo (5 nm)/Au (15 nm) thin film, where the experimental (Exp), calculated (Cal), and the differences are indicated (Exp−Cal). The Au and FeCo individual phases are also showed. Part (c) represents the X-ray reflectometry (XRR) measurement for the FeCo (5 nm)/Au (15 nm) thin film. In the inset, a schematic view of our system is indicated.

In contrast with standard surface calculations,[51] we relaxed the interlayer distances among the layers and the planar lattice constants using constrained stress tensor calculations for each slab with the aim to obtain an average lattice constant, a_{av}, as a function of the number of layers in the slab. For this task, we employed the effective coordination number (ECN) concept,[52] which provides the average interatomic distance d_{av}. As the bulk Au adopts a fcc structure, the average lattice constant can be estimated as $a_{av} = \sqrt{2}\, d_{av}$.

Using the FeCo composition employed in the experiments, namely, $Fe_{20\%}Co_{80\%}$, we construct a slab with 3 × 3 bcc(110) surfaces, 5 layers (9 Fe and 36 Co atoms), and a random distribution of the Fe and Co based on the special quasirandom structure (SQS) method.[53,54] A vacuum layer of 15 Å separates the periodic images of the slabs. With the aim to obtain the unstrained geometry for the FeCo slab, we relaxed this system performing constrained stress tensor calculations, which affects the planar lattice parameters of the slab. This geometry was used as a reference to investigate the magneto-elastic properties for the FeCo alloy, once the lattice strain is introduced by the modification of the planar lattice constants using scaling factors from 0.97 up to 1.03, corresponding to strains from −3 up to 3%. The geometries were fully relaxed for each value of strain. Further computational details, a detailed description of the effective coordination concept, and the atomic positions of the relaxed and unstrained FeCo alloy are reported in the Supporting Information.

4. RESULTS AND DISCUSSION

4.1. Structural Characterization. Figure 1a,c shows the room-temperature grazing incidence XRD (GIXRD) patterns of the FeCo (5 nm)/Au (5−20 nm) thin films and the XRR measurement for the FeCo (5 nm)/Au (15 nm) thin film, respectively. The last confirms the multilayer thicknesses, where the fit (red line) was done considering three layers as exhibited in the inset of Figure 1c, and using Parratt's formalism-based package. The obtained values of the thicknesses of the Au (14 ± 2 nm) and FeCo (3 ± 2 nm) after the fit are in agreement with the nominal values determined by the quartz crystal microbalance throughout the deposition. Meanwhile, the fist visual inspection of the fwhm of the diffraction peaks in Figure 1a displays a decreasing tendency as the thickness increases. This effect can be attributed to both residual strain and/or grain size modifications, as it is discussed subsequently. The analysis of the Bragg-peak positions allowed the identification of Au-phase (space group $Fm\bar{3}m$) and FeCo-phase (space group $Pm\bar{3}m$)

Table 1. Structural Parameters Obtained by Rietveld Refinement: Lattice Parameters, *a*, Fe−Co Average Bond Lengths, d_{Fe-Co}, Mean Grain Size, ⟨*D*⟩, and Residual Strain

gold thickness (nm)	*a* (Au) (Å)	*a* (FeCo) (Å)	d_{Fe-Co} (Å)	⟨*D*⟩ (Au) (nm)	strain (Au) (%)	strain (FeCo) (%)
5	4.0720 ± 0.0014	2.8241 ± 0.0026	2.4458	4.8(5)	1.5408	0.8150
10	4.0743 ± 0.0008	2.8272 ± 0.0024	2.4487	6.0(5)	0.7801	1.1961
15	4.0771 ± 0.0003	2.8326 ± 0.0019	2.4613	10.6(5)	0.7784	2.4419
20	4.0787 ± 0.0002	2.8405 ± 0.0015	2.4833	11.0(5)	0.7745	3.0816

DOI: 10.1021/acsami.8b14736
ACS Appl. Mater. Interfaces 2019, 11, 1529−1537

formation. The [111] and [110] reflections are the highest peaks in the Au and FeCo phase, respectively.

Rietveld refinements were performed on the GXRD patterns, using the Lorentzian function, which is implemented within the GSAS software. A typical refinement of the FeCo (5 nm)/Au (15 nm) thin film is shown in Figure 1b, where the observed and calculated intensity data are denoted by *Y* Exp and *Y* Calc, respectively. The solid line in the bottom represents the difference between them (*Y* Exp−Calc). Individual calculated diffraction patterns for Au and FeCo are also shown. The results are displayed in Table 1. The lattice parameters for both polycrystalline phases show a clear dependence of the gold thickness increase; see Table 1.[55,56] The lattice parameter of the gold phase increases, getting close to gold bulk's lattice value because of the lattice relaxation effect by the thickness increase.[57] There is a surface residual strain for each thickness of the Au underlayer, which is reflected on the grain size and coalescence stress resulting from the nucleation and the growth processes during formation of polycrystalline thin films. The last is inherited by the FeCo slab.

As is shown, an increase in the strain of the gold underlayer leads to a decrease in its lattice constant, while the structural parameters of the deposited FeCo tag along with this reduction due to intermetallic interface elastic processes, consequently a reduction of the Fe−Co average bond lengths. Moreover, it is worth to note that the FeCo phase shows a strong increase rate of its lattice parameter when compared with the gold phase one. This behavior is clearly observed by the relative variation of the lattice parameter, $\Delta a/a$, of the gold (≈0.16%) compared with the FeCo phase (≈0.58%). Meanwhile, the mean grain size $\langle D \rangle$ of the gold phase shows an increase with the gold thickness along with the reduction of its residual strain, as shown in Table 1. This behavior suggests that the crystallinity of the gold phase is significantly improved with an increment of its thicknesses, driven by the diffusion on grain boundaries. Similar behaviors were reported in the literature, such as in Al[58] and InP[59] films. As a result of the increase of the gold thickness, the FeCo strain shows an increasing behavior inherited by the gold-phase relaxation.

4.2. Magnetic Properties of the FeCo Alloy. Hysteresis loops at room temperature were carried out for all four samples' thickness, and the experimental results for these measurements are presented in Table 2. As can be seen, the

Table 2. Magnetic Saturation, M_s, and Coercivity Magnetic Field, H_c, Magnetic Anisotropy Field, H_K, and Anisotropy Energy, K_u, Obtained by the Loops as a Function of the Gold Thikness, ω

Ω (nm)	M_s emu/cm^3	H_c (Oe)	H_K (Oe)	K_u 10^5 erg/cm^3
5	4805	143(5)	477(30)	11.4
10	5129	113(5)	411(30)	9.9
15	4920	49(5)	382(30)	9.2
20	3560	25(5)	329(30)	5.4

magnetic saturation, M_s, shows a slightly variation, which can be attributed to changes in the strain. Figure 2 shows the room-temperature magnetization, *M*, versus magnetic field, *H*, in-plane for the easy and hard axis for all samples. The coercivity field for the thinner film ≈143 Oe is higher to the expected for FeCo alloys prepared by a classical sputtering method[60] (50−100 Oe), concluding that a thin gold-

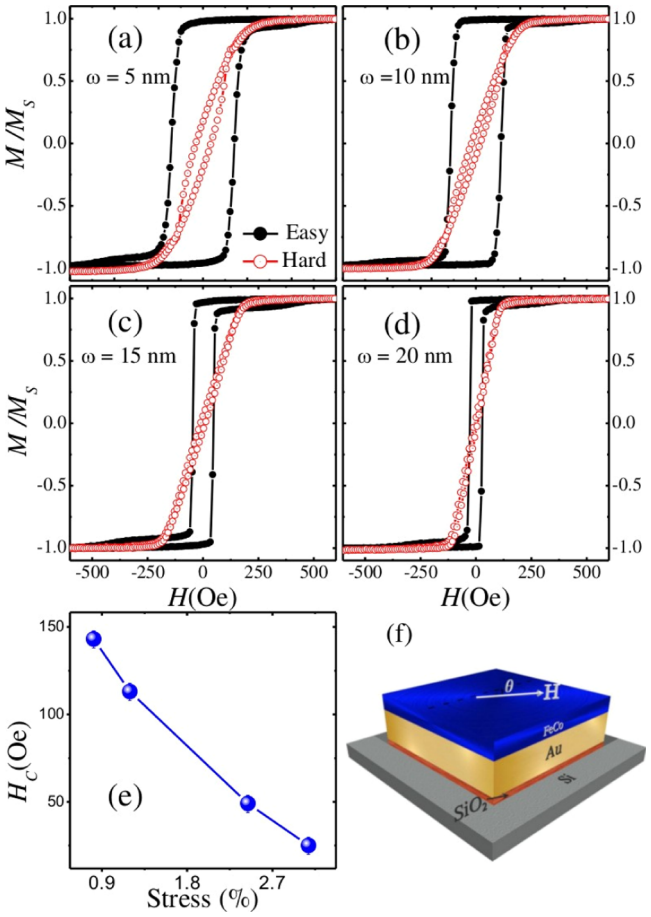

Figure 2. Normalized magnetization, M/M_s, as a function of the applied magnetic field, *H*, displayed by the easy and hard axis hysteresis loops from 5 to 20 nm gold-underlayer thickness (a−d). (e) Dependence of the coercivity field with the mean grain size and the residual strain of the FeCo phase obtained by XRD. (f) 3D full system showing the direction of the applied magnetic field.

underlayer can increase the H_c. At the same time, for subsequent thicknesses, the coercivity field reflects a progressive decreasing, as shown in Table 2, which strongly suggests a tuning of the coercive field by the control of the underlayer thickness. Furthermore, the anisotropy field, H_k, and the anisotropy energy, K_u, decrease as the gold thickness increases, which were calculated through the hard hysteresis loop (field which magnetization reach the saturation) and $K_u = M_s H_k/2$, respectively.

In order to correlate the strong dependence of the magnetic properties of the FeCo film induced by gold-underlayer thickness, the structural characterization was performed by XRD. A clear coercivity dependence can be seen in the inset of Figure 2d on the residual strain of the FeCo alloy. This behavior is in agreement with the magnetoelastic effect due to the internal strain,[26,27] originated by the mismatch of the lattice parameters of the Au and FeCo.

The surface topography characterization was performed in the both extremes of the thin films and determined by the AFM measurements, as is shown in Figure 3a,b. In these images, a notary surface roughness decrease is clearly observed, and this reduction is quantified and estimated to be 4.8 to 2.6 nm as the Au thickness increases, which is in agreement with the relief of the residual strain of the gold phase, inducing a bigger residual stress of the FeCo phase observed by XRD

DOI: 10.1021/acsami.8b14736
ACS Appl. Mater. Interfaces 2019, 11, 1529−1537

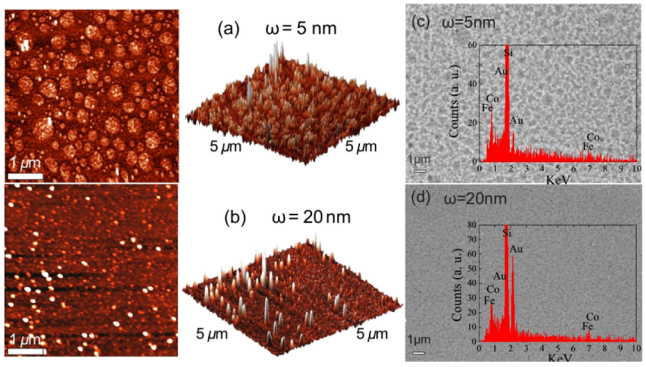

Figure 3. (a,b) Top and lateral view of the AFM images for 5 and 20 nm Au-underlayer/FeCo films, respectively. (c,d) Corresponding top view of the SEM images. In the insets, the elemental EDS analyses are included.

measurements. Additionally, scanning electron microscopy (SEM) images were carried out in the above analyzed samples (w = 5 nm and w = 20 nm), as shown in Figure 3c,d, and after a visual inspection, the film with a thinner gold-underlayer presents a more black-white contrast, which can be associated with more roughness observed by AFM measurements. Also, energy-dispersive spectroscopy (EDS) measurements were carried out in both samples in order to analyze the chemical composition, and those of Si, Co, Fe, and Au were determined; the Si element was associated with the silicon substrate. On the other hand, special attention can be given to the Au peak located at 2.2 keV, which displays a clear increase; this fact is in good concordance with the gold-underlayer phase thickness increase.

Figure 4 shows the room-temperature CEMS for the FeCo (5 nm)/Au (5 nm) film. The fit of the Mössbauer spectrum

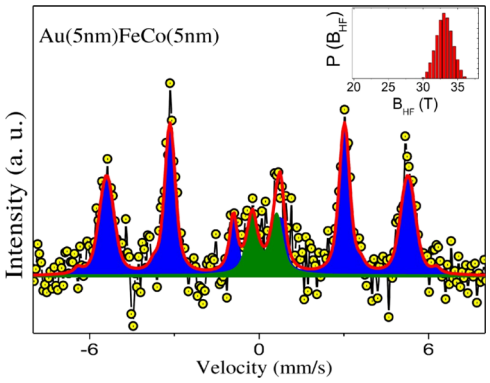

Figure 4. Room-temperature CEMS spectra corresponding to the FeCo (5 nm)/Au (5 nm) film. The continuous curves represent the best fit to the experimental data obtained by two distributions, corresponding to sextet and doublet distributions. The inset represents the magnetic hyperfine probability of the sextet distribution.

was carried out using the histogram method of the NORMOS DIST program, and it is fitting with two distributions, one corresponding to a sextet because of magnetically ordered Fe ions in a layer (84%), with mean magnetic hyperfine field, B_{hf}, at 33 T, isomer shift (δ) at 0.00 mm s^{-1} and linewidths (Γ) at 0.29 mm s^{-1}, which are in good agreement with $Fe_{20\%}Co_{80\%}$.[61] Furthermore, the angle, θ, formed by the Mössbauer γ-ray direction and the hyperfine magnetic field give information of the anisotropy direction,[62] which can be obtained by means of the relative intensities R_{23} of the lines 2 and 3 (or lines 5 and 4), which is 4 sin $2\theta/(1 + \cos(2\theta))$. Mössbauer spectra is undoubtedly a fingerprint of the in-plane magnetic field response shown in the previous Hysteresis plots. Hence, it reinforces our argument about the parallel or in-plane magnetic anisotropy.

This value was esteemed at ~75°, evidencing the majority in-plane anisotropy, according to the magnetic measurements. Likewise, this result is in agreement with the magnetic force microscopy images (Figure S2), where for the FeCo (5 nm)/Au (5 nm) film shows weak magnetic domain in-plane configuration, which is decreasing as the increase of the gold underlayer thickness, those show weak perpendicular anisotropy, which decreases with the increase of the gold. On the other hand, the other distribution of doublets, shown in Figure 4 (16%), evidences paramagnetic Fe^{3+} ions probably located in the interface region.[63]

4.3. Ab Initio Investigation of the Au(111) Underlayer. From the experimental characterization, we obtained a dependence of the lattice parameter of the Au-underlayer on its thickness, as shown in Table 1, which is a crucial result to explain the behavior of the magnetic FeCo properties. Our samples were grown using the magnetron sputtering technique, and hence, there are two possible origins for the changes: (i) the existence of a surface and (ii) the presence of intrinsic defects, such as vacancies. Thus, we check these two possibilities using ab initio calculations.

First, aiming to understand the dependence of the lattice parameter on the slab thickness, we changed the number of gold layers from 3 to 15 in the slab and obtained the evolution of the average lattice parameter, a_{av}, with the slab thickness, ω, for the fully relaxed structures in Figure 5a, where the

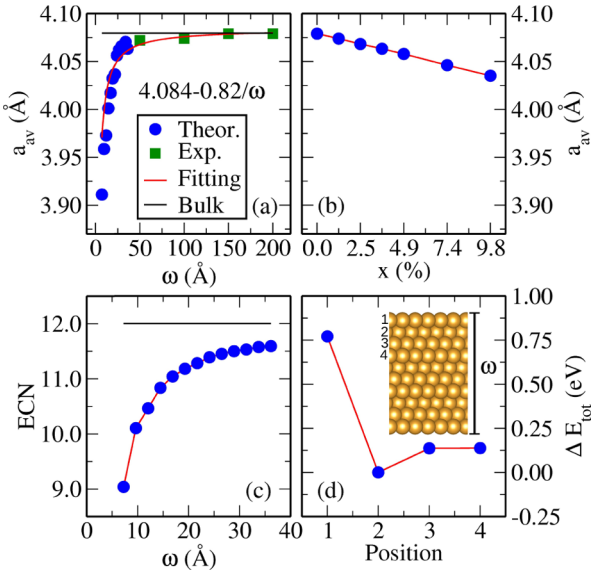

Figure 5. Ab initio calculations for the gold underlayer. (a,c) Investigation of the lattice parameter and ECN as a function of the gold thickness (ω). Theoretical values are represented by blue circles, whereas experimental data are represented by green squares. The inset in panel (a) shows an expression for a_{av} in Å. Panel (b) shows the lattice parameter as a function of the vacancy concentration for the Au bulk (without surfaces). In panel (d), the relative energy for Au monovacancies created in the first four layers of the Au(111) surface is shown.

DOI: 10.1021/acsami.8b14736
ACS Appl. Mater. Interfaces 2019, 11, 1529−1537

theoretical results are represented by circles, and the experimental measurements were represented by squares. Usually, the PBE functional overestimates[46] the bond length up to about 2%, and hence, we multiply the DFT-PBE lattice parameter by a scaling factor $f = a_0^{Exp}/a_0^{PBE}$, where a_0^{Exp} (a_{PBE}) is the lattice parameter for Au bulk obtained from the experiment (DFT calculations).

Such a procedure was necessary to allow a direct comparison between theory and experiment. Despite the experimental results already showing a trend of the lattice parameter, that is, growing as the sample thickness increases, we predict a dramatic change of the lattice parameter as the number of layers decrease, which could be verified even experimentally by a more precise atomic layer by layer laser molecular beam epitaxy. Both of them, the theoretic and experimental data, were fitted by a plain hyperbolic law which accounts for the behavior of the lattice parameter from the bulk to the few layers regime.

As mentioned, the presence of point defects is another possible source of changes in the lattice parameter of the Au-underlayer. Thus, in order to investigate this possibility, we employed a 3 × 3 × 9 Au periodic supercell and created monovacancies, removing Au atoms from it in positions which are randomly determined. Note that in this particular set of calculations, we employed the supercell approach without surfaces, neglecting the surface effects. Later, to optimize the volume of the supercell with stress tensor calculations, we calculated the evolution of the average lattice parameter, a_{av}, with the monovacancy concentration x, depicted in panel (b) of Figure 5. Our results demonstrated a subtle decrease of a_{av} with x, leading us to conclude that the presence of defects shortens bond lengths, being an additional factor for the surface effects presented in panel (a). However, high vacancy concentrations were necessary to generate larger variations in a_{av}.

We investigated also the case in which a vacancy is located in the outermost surface layers. For that, we employed a 3 × 3 Au(111) surface unit cell with nine layers in the slab and created a single vacancy in several positions surrounding the surface. All these calculations were relaxed with constrained stress tensor calculations. In Figure 5d, we show the relative energy of a monovacancy as a function of its position, that is, close to the surface of the inner layers of the Au(111) surface. From our DFT calculations, we conclude that the monovacancies positioned in the outermost layer are highly energetically unfavorable, being 0.75 eV higher in energy in comparison to monovacancies in the layer neighboring the edge layer, which is the lowest energy position. Furthermore, defects created in the bulk region are 0.12 eV more energetic in comparison with the ground state. Considering that monovacancies at the surface miss 9 chemical bonds, whereas inner monovacancies miss 12 chemical bonds, the number of chemical bonds plays a fundamental role in the energetic stabilization of Au thin films.

The shortening of the lattice parameter demonstrated in the experiments and corroborated with DFT-PBE calculations could be straightforwardly understood, considering the metallic nature of the chemical bonds in Au. In the Au bulk, each atom contributes with one ($6s^1$) valence electron and makes 12 chemical bonds. Thus, each chemical bond is established by 2/12 electrons once two Au atoms are involved. However, for the surface gold layers, the Au atoms have only nine chemical bonds, despite maintaining the number of valence electrons. Such a situation increases the number of electrons per chemical bond in the overall system, resulting in an enhancement of the strength of each chemical bonds. The final effect is the shortening of the lattice parameter generated by a strengthening of the chemical bonds.

Thus, the presence of surfaces or defects leads to a decreasing of the average coordination, a_{av}, which will result in decreasing of its average lattice parameter. Figure 5c depicts the average ECN as a function of the layer thickness, showing that the ECN increases with the number of Au layers, tending to the bulk phase, that is, ECN = 12. Despite these calculations carried out for gold layers, these results can be extrapolated for polycrystalline thin films.

4.4. Theoretical Model for the FeCo Thin Film Alloy. Our experimental data show a bcc(110) surface of FeCo interfacing an fcc(111) surface of Au. The elastic effect that we are evidentiating in this work is a strain induced in the FeCo thin-film alloy which is originated by the lattice parameters of the Au-underlayer, being, as a matter of fact, an interface effect. However, the complexity of this interface is a drawback for an ab initio investigation, as we expect the presence of roughness and reconstructions at the interfaces. Furthermore, the Au-underlayer considered in our experiments reaches 20 nm in thickness, turning the explicit description of the FeCo/Au interfaces a problem highly complicated for ab initio simulations. Thus, to make the problem feasible, we investigate the effects of planar strain in the FeCo alloy without the explicit inclusion of the Au-underlayer. In this way, we can correlate the theoretical results with the experimental ones through the value of the strain.

Our theoretical model describing the FeCo alloy was constructed from the SQS methodology and consists of a slab with five layers. The FeCo slab width has 9.62 Å, which is much thinner than the experimentally realized alloy. Figure 6a

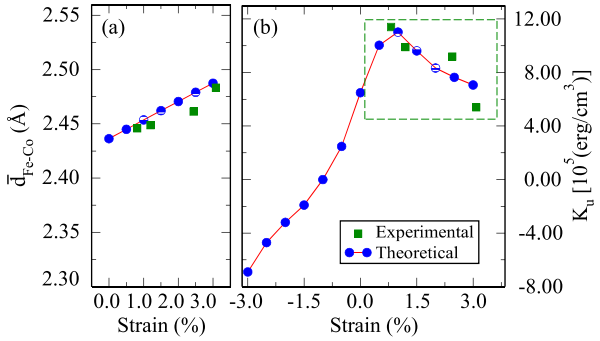

Figure 6. (a) Average Fe−Co bond lengths; (b) in-plane magnetic anisotropy energy as a function of the strain for the FeCo alloy. Theoretical values are represented by blue circles, whereas experimental data are represented by green squares.

compares the Fe−Co bond length, $\bar{d}_{Fe-Co}$, taken from theory and experiments. Despite some small deviations of less than 0.3%, there is a strong agreement, including the increasing of $\bar{d}_{Fe-Co}$ with similar slopes. Thus, it is expected that the theoretical model, despite its small width in comparison with the experimental realized one, will capture the main characteristics.

4.5. Tuning the Magnetic Anisotropy. In the potential utilization of the methods reported in this work in the fabrication of future magnetic devices, an important point is the magnetic anisotropy hardness. Because hard magnetic

DOI: 10.1021/acsami.8b14736
ACS Appl. Mater. Interfaces 2019, 11, 1529−1537

anisotropies are required to avoid the thermic loss of information, while at the same time soft magnetic anisotropies are wanted for fast data processing, a fine control of the hardness of the magnetic anisotropy is an essential challenge. In this regard, we present in this section our results for the magnetoelastic properties of the FeCo thin film alloy.

We find a high dependence of the in-plane magnetic anisotropy energy[3,64] on the planar strain of the FeCo alloy, accessed from both theory and experiments and shown in Figure 6b. The theoretical data for the magnetic anisotropy energy was obtained from the total energy difference between configurations with different spin orientations. In the particular case of the in-plane anisotropy, $K_u = E_{\parallel}^{x} - E_{\parallel}^{y}$, where $E_{\parallel}^{x(y)}$ is the total energy constraining the spin in the $x(y)$ direction.[64] Moreover, the SOC within the noncollinear spin approach was considered.[6] On the other hand, the experimental data for the magnetic anisotropy energy was calculated through a hard hysteresis loop, as discussed in Section 4.2. Additional experimental details are reported in the Supporting Information.

The region experimentally assessed was enclosed by the dashed box. Again, we found an excellent agreement between theory and experiment, demonstrating the suitability of the theoretical model proposed in this work. In addition, beyond experimental data's availability region, we also investigated the K_u for the strain in the compressing regime. Surprisingly, the DFT calculations predicted a rich K_u spectrum. Thus, the handling of the magnetic properties via an underlayer width could control not only the hardness of the magnetic anisotropy but also the direction of the magnetization of the FeCo/Au systems. Such a controlling mechanism opens several possibilities for applications in future devices, as memories, with the possibility of large-scale fabrication.

5. CONCLUSIONS

In summary, polycrystalline thin films of FeCo (≈5 nm) were grown on the Au-underlayer with thicknesses up to 20 nm by a magnetron sputtering technique. We found that the magnetic properties of the FeCo alloy is controlled by their FeCo strain inherited by the golden phase. These behaviors were associated with the magnetoelastic effect. Systematic ab initio simulations of the Au-underlayer reveal that the presence of the surface and vacancies in thinner gold films are a ruling factor to the reduction of its lattice constant. Also, for the values of strain accessed in our experiments, 0.8−3.1%, we found that the measures of the magnetic anisotropy energy are in good accordance with theoretical calculations performed with a free-standing FeCo alloy. Such agreement shows that despite the presence of grain boundaries and a FeCo/Au interface, the strain is the most important factor for the tuning of the magnetic anisotropy energy.

In addition, analyzing the theoretical K_u beyond the experimental data availability region, we predicted a rich K_u dependence on the strain, allowing a strain-driven control of both the intensity and the direction of the magnetic anisotropy. The mechanism proposed in this work can be extended, systematically, to other alloy compositions deposited on different metallic underlayers, opening the possibility of growth systems with a desirable magnetic properties using a technique allowing large-scale production.

■ ASSOCIATED CONTENT

Supporting Information

The Supporting Information is available free of charge on the ACS Publications website at DOI: 10.1021/acsami.8b14736.

Further computational details and the FeCo alloy geometry (PDF)

■ AUTHOR INFORMATION

Corresponding Author

*E-mail: juarez_dasilva@iqsc.usp.br.

ORCID

Luís Cabral: 0000-0002-4834-0552
Leonardo Villegas-Lelovsky: 0000-0002-3408-3612
Matheus P. Lima: 0000-0001-5389-7649
Juarez L. F. Da Silva: 0000-0003-0645-8760

Notes

The authors declare no competing financial interest.

■ ACKNOWLEDGMENTS

We thank E. D. Guarin Castro for technical assistance with the figures. The computational simulations were performed using the computational resources of the Centro de Ciências Matemáticas Aplicadas à Indústria (CeMEAI) supported by FAPESP (São Paulo Research Foundation). W.A.A.M. acknowledges the CNPq (grants 502042/2013-3, 30834/2014-6 and 426937/2016-3) and Fapemig (grant PPM-00431-17). J.L.F.D.S. gratefully acknowledges support from FAPESP (grant number 2017/11631-2), Shell and the strategic importance of the support given by ANP (Brazils National Oil, Natural Gas and Biofuels Agency) through the R&D levy regulation. This study was financed in part by the Coordenação de Aperfeiçoamento de Pessoal de Nível Superior—Brasil (CAPES)—Finance Code 001.

■ ABBREVIATIONS

dc, direct current
GXRD, grazing angle X-ray diffraction
GSAS, General Structure Analysis System
AFM, atomic force microscopy
CEMS, conversion electron Mössbauer spectroscopy
DFT, density functional theory
PBE, Perdew−Burke−Ernzerhof
VASP, Vienna Ab initio Simulation Package
SQS, special quasirandom structure

■ REFERENCES

(1) Yang, H.; Vu, A. D.; Hallal, A.; Rougemaille, N.; Coraux, J.; Chen, G.; Schmid, A. K.; Chshiev, M. Anatomy and Giant Enhancement of the Perpendicular Magnetic Anisotropy of Cobalt-Graphene Heterostructures. *Nano Lett.* **2015**, *16*, 145−151.

(2) Rau, I. G.; Baumann, S.; Rusponi, S.; Donati, F.; Stepanow, S.; Gragnaniello, L.; Dreiser, J.; Piamonteze, C.; Nolting, F.; Gangopadhyay, S.; Albertini, O. R.; Macfarlane, R. M.; Lutz, C. P.; Jones, B. A.; Gambardella, P.; Heinrich, A. J.; Brune, H. Reaching the magnetic anisotropy limit of a 3d metal atom. *Science* **2014**, *344*, 988−992.

(3) Yang, H.; Vu, A. D.; Hallal, A.; Rougemaille, N.; Coraux, J.; Chen, G.; Schmid, A. K.; Chshiev, M. Anatomy and Giant Enhancement of the Perpendicular Magnetic Anisotropy of Cobalt-Graphene Heterostructures. *Nano Lett.* **2015**, *16*, 145−151.

DOI: 10.1021/acsami.8b14736
ACS Appl. Mater. Interfaces 2019, 11, 1529−1537

(4) Łusakowski, A.; Szuszkiewicz, W. Ab Initio Studies of Magnetic Anisotropy Energy in Highly Co-Doped ZnO. *J. Magn. Magn. Mater.* **2017**, *426*, 479−482.
(5) Lau, Y.-C.; Sheng, P.; Mitani, S.; Chiba, D.; Hayashi, M. Electric Field Modulation of the Non-Linear Areal Magnetic Anisotropy Energy. *Appl. Phys. Lett.* **2017**, *110*, 022405.
(6) Steiner, S.; Khmelevskyi, S.; Marsmann, M.; Kresse, G. Calculation of the Magnetic Anisotropy with Projected-augmented-wave Methodology and the Case Study of Disordered Fe1−xCoxAlloys. *Phys. Rev. B* **2016**, *93*, 224425.
(7) Cao, D.; Zhu, Z.; Feng, H.; Pan, L.; Cheng, X.; Wang, Z.; Wang, J.; Liu, Q. Applied Magnetic Field Angle Dependence of the Static and Dynamic Magnetic Properties in FeCo Films During the Deposition. *J. Magn. Magn. Mater.* **2016**, *416*, 208−212.
(8) Li, J.; Zhan, Q.; Zhang, S.; Wei, J.; Wang, J.; Pan, M.; Xie, Y.; Yang, H.; Zhou, Z.; Xie, S.; Wang, B.; Li, R.-W. Magnetic Anisotropy and High-frequency Property of Flexible FeCoTa Films Obliquely Deposited on a Wrinkled Topography. *Sci. Rep.* **2017**, *7*, 2837.
(9) Choi, K. J.; Biegalski, M.; Li, Y. L.; Sharan, A.; Schubert, J.; Uecker, R.; Reiche, P.; Chen, Y. B.; Pan, X. Q.; Gopalan, V.; Chen, L.-Q.; Schlom, D. G.; Eom, C. B. Enhancement of Ferroelectricity in Strained BaTiO3 Thin Films. *Science* **2004**, *306*, 1005−1009.
(10) Sando, D.; Yang, Y.; Bousquet, E.; Carrétéro, C.; Garcia, V.; Fusil, S.; Dolfi, D.; Barthélémy, A.; Ghosez, P.; Bellaiche, L.; Bibes, M. Large Elasto−optic Effect and Reversible Electrochromism in Multiferroic BiFeO3. *Nat. Commun.* **2016**, *7*, 10718.
(11) Huang, B.; Jin, K.-H.; Cui, B.; Zhai, F.; Mei, J.; Liu, F. Bending Strain Engineering in Quantum Spin Hall System for Controlling Spin Currents. *Nat. Commun.* **2017**, *8*, 15850.
(12) Wu, S. Z.; Miao, J.; Xu, X. G.; Yan, W.; Reeve, R.; Zhang, X. H.; Jiang, Y. Strain-mediated Electric-field Control of Exchange Bias in a Co90Fe10/BiFeO3/PMN-PT Heterostructure. *Sci. Rep.* **2015**, *5*, 8905.
(13) Wen, K.; Lv, W.; He, W. Interfacial Lattice-strain Effects on Improving the Overall Performance of Micro-solid Oxide Fuel Cells. *J. Mater. Chem. A* **2015**, *3*, 20031−20050.
(14) Wen, K.; Zhang, K. H. L.; Wang, W.; Lin, J.; Lv, W.; Wang, B.; Wang, Z. M.; Dickerson, J. H.; Guo, X.; He, W. Physical Justification for Ionic Conductivity Enhancement at Strained Coherent Interfaces. *J. Power Sources* **2015**, *285*, 37−42.
(15) Wen, K.; Han, Y.; Zou, M.; Lv, W.; He, W. Interfacial Strain Effect on Gas Transport in Nanostructured Electrodes of Solid Oxide Fuel Cells. *J. Power Sources* **2015**, *291*, 126−131.
(16) Han, Y.; Jing, X.; Zhou, X.; Zhang, K. H.; Li, S.; Wang, W.; He, W. Coordination-dependent Surface Strain and Rational Construction of Robust Structures. *Nanotechnology* **2018**, *29*, 465708.
(17) Sun, S.; Murray, C. B.; Weller, D.; Folks, L.; Moser, A. Monodisperse FePt Nanoparticles and Ferromagnetic FePt Nanocrystal Superlattices. *Science* **2000**, *287*, 1989−1992.
(18) Chaubey, G. S.; Barcena, C.; Poudyal, N.; Rong, C.; Gao, J.; Sun, S.; Liu, J. P. Synthesis and Stabilization of FeCo Nanoparticles. *J. Am. Chem. Soc.* **2007**, *129*, 7214−7215.
(19) Xu, Y.-H.; Wang, J.-P. FeCo-Au core-shell nanocrystals. *Appl. Phys. Lett.* **2007**, *91*, 233107.
(20) Lafford, T. A.; Gibbs, M. R. J.; Shearwood, C. Magnetic, magnetostrictive and structural properties of iron-cobalt/silver multilayers. *J. Magn. Magn. Mater.* **1994**, *132*, 89−94.
(21) Lafford, T. A.; Gibbs, M. R. J.; Zuberek, R.; Shearwood, C. Magnetostriction and magnetic properties of iron-cobalt alloys multilayered with silver. *J. Appl. Phys.* **1994**, *76*, 6534−6536.
(22) Wang, L. C.; Hatton, H. J.; Cooke, M. D.; Gibbs, M. R. J.; Rainforth, W. M.; Hetherington, C. J. D. Microstructure and Magnetoelastic Properties of FeCo/Ag Multilayers. *J. Appl. Phys.* **2001**, *89*, 7511−7513.
(23) Wu, D.; Zhang, Q.; Liu, J. P.; Yuan, D.; Wu, R. First-principles Prediction of Enhanced Magnetic Anisotropy in FeCo Alloys. *Appl. Phys. Lett.* **2008**, *92*, 052503.
(24) Gong, M.; Kirkeminde, A.; Wuttig, M.; Ren, S. Phase Transformation-Induced Tetragonal FeCo Nanostructures. *Nano Lett.* **2014**, *14*, 6493−6498.
(25) Li, D.; Li, Y.; Pan, D.; Zhang, Z.; Choi, C.-J. Prospect and Status of Iron-based Rare-earth-free Permanent Magnetic Materials. *J. Magn. Magn. Mater.* **2019**, *469*, 535−544.
(26) Lu, Z.; Fukuma, Y.; Butler, W. H.; Fujiwara, H.; Mankey, G. J.; Matsunuma, S. Magnetic Anisotropy of FeCo Films Induced by Obliquely Sputtered Ru Underlayers. *IEEE Trans. Magn.* **2009**, *45*, 4008−4010.
(27) McMichael, R. D.; Lee, C. G.; Bonevich, J. E.; Chen, P. J.; Miller, W.; Egelhoff, W. F., Jr. Strong Anisotropy in Thin Magnetic Films Deposited on Obliquely Sputtered Ta Underlayers. *J. Appl. Phys.* **2000**, *88*, 5296−5299.
(28) Winkelmann, A.; Przybylski, M.; Luo, F.; Shi, Y.; Barthel, J. Perpendicular Magnetic Anisotropy Induced by Tetragonal Distortion of FeCo Alloy Films Grown on Pd(001). *Phys. Rev. Lett.* **2006**, *96*, 257205.
(29) Jian, X.; Wu, B.; Wei, Y.; Dou, S. X.; Wang, X.; He, W.; Mahmood, N. Facile Synthesis of Fe3O4/GCs Composites and Their Enhanced Microwave Absorption Properties. *ACS Appl. Mater. Interfaces* **2016**, *8*, 6101−6109.
(30) Jian, X.; Xiao, X.; Deng, L.; Tian, W.; Wang, X.; Mahmood, N.; Dou, S. Heterostructured Nanorings of Fe−Fe3O4@C Hybrid with Enhanced Microwave Absorption Performance. *ACS Appl. Mater. Interfaces* **2018**, *10*, 9369−9378.
(31) Żuberek, R.; Wawro, A.; Szymczak, H.; Wisniewski, A.; Paszkowicz, W.; Gibbs, M. R. J. Magnetostriction and Magnetic Anisotropy of FeCo/Au Multilayers. *J. Magn. Magn. Mater.* **2000**, *214*, 155−158.
(32) Konishi, Y.; Fang, Z.; Izumi, M.; Manako, T.; Kasai, M.; Kuwahara, H.; Kawasaki, M.; Terakura, K.; Tokura, Y. Orbital-State-Mediated Phase-Control of Manganites. *J. Phys. Soc. Jpn.* **1999**, *68*, 3790−3793.
(33) Sando, D.; Agbelele, A.; Rahmedov, D.; Liu, J.; Rovillain, P.; Toulouse, C.; Infante, I. C.; Pyatakov, A. P.; Fusil, S.; Jacquet, E.; Carrétéro, C.; Deranlot, C.; Lisenkov, S.; Wang, D.; Le Breton, J.-M.; Cazayous, M.; Sacuto, A.; Juraszek, J.; Zvezdin, A. K.; Bellaiche, L.; Dkhil, B.; Barthélémy, A.; Bibes, M. Crafting the magnonic and spintronic response of BiFeO3 films by epitaxial strain. *Nat. Mater.* **2013**, *12*, 641.
(34) van der Laan, G. Microscopic Origin of Magnetocrystalline Anisotropy in Transition Metal Thin Films. *J. Phys.: Condens. Matter* **1998**, *10*, 3239.
(35) Bansmann, J.; Baker, S.; Binns, C.; Blackman, J.; Bucher, J.; Dorantesdavila, J.; Dupuis, V.; Favre, L.; Kechrakos, D.; Kleibert, A.; Meiwes-Broer, K.-H.; Pastor, G.; Perez, A.; Toulemonde, O.; Trohidou, K. N.; Tuaillon, J.; Xie, Y. Magnetic and Structural Properties of Isolated and Assembled Clusters. *Surf. Sci. Rep.* **2005**, *56*, 189−275.
(36) Reiss, G.; Hütten, A. Applications Beyond Data Storage. *Nat. Mater.* **2005**, *4*, 725.
(37) Reim, W.; Gambino, R. J.; Ruf, R. R.; Plaskett, T. S. TbxNdy(FeCo)1−x−y: Promising materials for magneto-optical storage? *J. Appl. Phys.* **1987**, *61*, 3349−3351.
(38) Burkert, T.; Nordström, L.; Eriksson, O.; Heinonen, O. Giant Magnetic Anisotropy in Tetragonal FeCo Alloys. *Phys. Rev. Lett.* **2004**, *93*, 027203.
(39) Mansuripur, M.; Sincerbox, G. Principles and Techniques of Optical Data Storage. *Proc. IEEE* **1997**, *85*, 1780−1796.
(40) Lehnert, A.; Dennler, S.; Błoński, P.; Rusponi, S.; Etzkorn, M.; Moulas, G.; Bencok, P.; Gambardella, P.; Brune, H.; Hafner, J. Magnetic Anisotropy of Fe and Co Ultrathin Films Deposited on Rh(111) and Pt(111) Substrates: An Experimental and First−principles Investigation. *Phys. Rev. B: Condens. Matter Mater. Phys.* **2010**, *82*, 094409.
(41) Kleibert, A.; Bulut, F.; Gebhardt, R. K.; Rosellen, W.; Sudfeld, D.; Passig, J.; Bansmann, J.; Meiwes-Broer, K. H.; Getzlaff, M. Correlation of shape and magnetic anisotropy of supported mass-

DOI: 10.1021/acsami.8b14736
ACS Appl. Mater. Interfaces 2019, 11, 1529−1537

filtered Fe and FeCo alloy nanoparticles on W(110). *J. Phys.: Condens. Matter* **2008**, *20*, 445005.
(42) Larson, A.; Dreele, R. V. General Structure Analysis System (GSAS). *Report Laur*, 2000; Vol. *86*.
(43) Perdew, J. P.; Burke, K.; Ernzerhof, M. Generalized Gradient Approximation Made Simple. *Phys. Rev. Lett.* **1996**, *77*, 3865−3868.
(44) Lejaeghere, K.; Bihlmayer, G.; Bjorkman, T.; Blaha, P.; Blugel, S.; Blum, V.; Caliste, D.; Castelli, I. E.; Clark, S. J.; Dal Corso, A.; de Gironcoli, S.; Deutsch, T.; Dewhurst, J. K.; Di Marco, I.; Draxl, C.; Duak, M.; Eriksson, O.; Flores-Livas, J. A.; Garrity, K. F.; Genovese, L.; Giannozzi, P.; Giantomassi, M.; Goedecker, S.; Gonze, X.; Granas, O.; Gross, E. K. U.; Gulans, A.; Gygi, F.; Hamann, D. R.; Hasnip, P. J.; Holzwarth, N. A. W.; Iuan, D.; Jochym, D. B.; Jollet, F.; Jones, D.; Kresse, G.; Koepernik, K.; Kucukbenli, E.; Kvashnin, Y. O.; Locht, I. L. M.; Lubeck, S.; Marsman, M.; Marzari, N.; Nitzsche, U.; Nordstrom, L.; Ozaki, T.; Paulatto, L.; Pickard, C. J.; Poelmans, W.; Probert, M. I. J.; Refson, K.; Richter, M.; Rignanese, G.-M.; Saha, S.; Scheffler, M.; Schlipf, M.; Schwarz, K.; Sharma, S.; Tavazza, F.; Thunstrom, P.; Tkatchenko, A.; Torrent, M.; Vanderbilt, D.; van Setten, M. J.; Van Speybroeck, V.; Wills, J. M.; Yates, J. R.; Zhang, G.-X.; Cottenier, S. Reproducibility in Density Functional Theory Calculations of Solids. *Science* **2016**, *351*, aad3000.
(45) Sarker, D.; Bhattacharya, S.; Srivastava, P.; Ghosh, S. Triggering of Spin-flipping-modulated Exchange Bias in FeCo Nanoparticles by Electronic Excitation. *Sci. Rep.* **2016**, *6*, 39292.
(46) Zhang, Y.; Sun, J.; Perdew, J. P.; Wu, X. Comparative First−principles Studies of Prototypical Ferroelectric Materials by LDA, GGA, and SCAN Meta-GGA. *Phys. Rev. B* **2017**, *96*, 035143.
(47) Blöchl, P. E. Projector augmented-wave method. *Phys. Rev. B: Condens. Matter Mater. Phys.* **1994**, *50*, 17953−17979.
(48) Kresse, G.; Joubert, D. From Ultrasoft Pseudopotentials to the Projector Augmented-Wave Method. *Phys. Rev. B: Condens. Matter Mater. Phys.* **1999**, *59*, 1758−1775.
(49) Kresse, G.; Hafner, J. Ab initiomolecular dynamics for open-shell transition metals. *Phys. Rev. B: Condens. Matter Mater. Phys.* **1993**, *48*, 13115−13118.
(50) Kresse, G.; Furthmüller, J. Efficient iterative schemes forab initiototal-energy calculations using a plane-wave basis set. *Phys. Rev. B: Condens. Matter Mater. Phys.* **1996**, *54*, 11169−11186.
(51) Freire, R. L. H.; Kiejna, A.; Da Silva, J. L. F. Adsorption of Rh, Pd, Ir, and Pt on the Au(111) and Cu(111) Surfaces: A Density Functional Theory Investigation. *J. Phys. Chem. C* **2014**, *118*, 19051−19061.
(52) Da Silva, J. L. F. Effective Coordination Concept Applied for Phase Change $(GeTe)_m(Sb2Te3)_n$ Compounds. *J. Appl. Phys.* **2011**, *109*, 023502.
(53) Wei, S.-H.; Ferreira, L. G.; Bernard, J. E.; Zunger, A. Electronic Properties of Random Alloys: Special Quasirandom Structures. *Phys. Rev. B: Condens. Matter Mater. Phys.* **1990**, *42*, 9622−9649.
(54) Zunger, A.; Wei, S.-H.; Ferreira, L. G.; Bernard, J. E. Special Quasirandom Structures. *Phys. Rev. Lett.* **1990**, *65*, 353−356.
(55) Huang, C.-J.; Chiu, P.-H.; Wang, Y.-H.; Chen, K.-L.; Linn, J.-J.; Yang, C.-F. Electrochemically Controlling the Size of Gold Nanoparticles. *J. Electrochem. Soc.* **2006**, *153*, D129−D133.
(56) Davey, W. P. Precision Measurements of the Lattice Constants of Twelve Common Metals. *Phys. Rev.* **1925**, *25*, 753−761.
(57) Kolská, Z.; Říha, J.; Hnatowicz, V.; Švorčík, V. Lattice parameter and expected density of Au nano-structures sputtered on glass. *Mater. Lett.* **2010**, *64*, 1160−1162.
(58) Lita, A. E.; Sanchez, J. E., Jr. Characterization of Surface Structure in Sputtered Al Films: Correlation to Microstructure Evolution. *J. Appl. Phys.* **1999**, *85*, 876−882.
(59) Öztas, M. Influence of Grain Size on Electrical and Optical Properties of InP Films. *Chin. Phys. Lett.* **2008**, *25*, 4090.
(60) Cakmaktepe, S.; Coskun, M. I.; Yildiz, A. Underlayer Effect on Structural and Magnetic Properties of Co90Fe10Thin Films. *Lith. J. Phys.* **2013**, *53*, 112−118.
(61) Jartych, E.; Olchowik, J.; Zurawicz, J. K.; Budzynski, M. A Mossbauer Spectroscopy Study of Electrodeposited (Cox Ni1−x)1−yFey Alloys with 0<or=x<or=1 and y<or=0.01. *J. Phys.: Condens. Matter* **1993**, *5*, 8921.
(62) Keune, W. Application of Mössbauer Spectroscopy in Magnetism. *Hyperfine Interact.* **2012**, *204*, 13−45.
(63) Paul, A.; Gupta, A. Effect of Interface Structure Modifications on the Properties of Some Magnetic Multilayers. *J. Alloys Compd.* **2001**, *326*, 246−250.
(64) Enkovaara, J.; Ayuela, A.; Nordström, L.; Nieminen, R. M. Magnetic Anisotropy in Ni2MnGa. *Phys. Rev. B: Condens. Matter Mater. Phys.* **2002**, *65*, 134422.

DOI: 10.1021/acsami.8b14736
ACS Appl. Mater. Interfaces 2019, 11, 1529−1537